PHYSICAL REVIEW E **79**, 041301 (2009)

Dynamics of gas-fluidized granular rods

L. J. Daniels,[1] Y. Park,[2] T. C. Lubensky,[1] and D. J. Durian[1]
[1]*Department of Physics and Astronomy, University of Pennsylvania, Philadelphia, Pennsylvania 19104-6396, USA*
[2]*Department of Physics, Myong Ji University, Yongin, Gyeonggido 449–728, Korea*

(Received 17 November 2008; published 1 April 2009)

We study a quasi-two-dimensional monolayer of granular rods fluidized by a spatially and temporally homogeneous upflow of air. By tracking the position and orientation of the particles, we characterize the dynamics of the system with sufficient resolution to observe ballistic motion at the shortest time scales. Particle anisotropy gives rise to dynamical anisotropy and superdiffusive dynamics parallel to the rod's long axis, causing the parallel and perpendicular mean-square displacements to become diffusive on different time scales. The distributions of free times and free paths between collisions deviate from exponential behavior, underscoring the nonthermal character of the particle motion. The dynamics show evidence of rotational-translational coupling similar to that of an anisotropic Brownian particle. We model rotational-translational coupling in the single-particle dynamics with a modified Langevin model using nonthermal noise sources. This suggests a phenomenological approach to thinking about collections of self-propelling particles in terms of enhanced memory effects.

DOI: 10.1103/PhysRevE.79.041301 PACS number(s): 45.70.−n, 47.55.Lm

I. INTRODUCTION

Flocking birds, schooling fish, and swarming bacteria are examples of collections of self-propelled particles—particles that take in energy from their environment and then dissipate it by moving in a preferential direction through that environment—that display collective coherent behavior over a huge range of length scales. A wealth of theoretical work, ranging from minimal rule-based models [1,2] to coarse-grained hydrodynamic theories that employ symmetry considerations [3–5], has been conducted in order to elucidate those behaviors that are universal to collections of self-propelled particles. The earliest physical model [1] predicted a phase transition from a disordered to a true long-range-ordered state in two dimensions, in direct contrast to thermal systems where such a transition is explicitly forbidden. For apolar particles with nematic order, the broken-symmetry phase is characterized by anomalously large number fluctuations [6,7]. Other modes of collective behavior predicted include swirling and vortex motion [8,9] and propagating waves [10–12].

Despite the abundance of models and simulations, little experiment on physical systems has been conducted, with what has been done focusing on vertically vibrated granular systems [9,13–17]. These systems afford an advantage over biological systems: there is control over the microscopics and energy input, and a steady state can typically be reached provided the system does not age. Vibrated-bed experiments have observed swirling vortices [9,13], pattern formation [14], and shape-dependent long-range ordering [15]. Recently, giant number fluctuations were observed in a vertically vibrated monolayer of nematic-ordered granular rods [16]. Large number fluctuations were also reported for a collection of vibrated spheres [18], fueling some debate [19] as to whether the large density fluctuations are due to the self-propelled nature of the particles, inelastic collisions, or a heaping instability [13] observed in vibrated media. Additionally, vertical vibration as a method of driving has several inherent disadvantages: the driving force is temporally inhomogeneous and the particle dynamics may vary depending on the phase of the oscillation cycle at the time the particle contacts the substrate. Furthermore, for spherical particles on smooth plates, a lateral force is only generated by particle overlap out of plane; particles "boosted" to high speeds in this manner contribute to power-law tails in velocity distributions.

In the interest of discerning universal characteristics of collections of self-propelled particles, we consider another method of driving. Here, we report on a quasi-two-dimensional monolayer of granular rods fluidized by an upflow of air. The fluidizing airflow is temporally and spatially homogeneous, with airspeed less than free fall and with Reynolds number much greater than one. Because of their extended shape, the particles move by scooting when one of their ends has lifted off the substrate. This results in self-propelled behavior characterized by dynamical anisotropy between translations parallel and perpendicular to the particle's long axis. To elucidate the effect of self-propulsion, we characterize the dynamics of a single particle and compare it to the behavior of an anisotropic Brownian particle [20–22]. To that end, we model our system using the same Langevin formalism as for a Brownian particle with a single modification: particle self-propulsion is included implicitly via nonthermal noise terms.

II. EXPERIMENTAL DETAILS

The system we study, depicted in Fig. 1(a), consists of a monolayer of 435 cylindrical plastic dowel pins—length $L=0.95$ cm, diameter $d=0.24$ cm, and mass $m=0.055$ g—fluidized by an upflow of air. The particular area fraction $\phi=42\%$ ensures that the particles are uniformly distributed across the system. The particle aspect ratio, $L/d=4$, is chosen to prevent any long-range ordering. Although an effective harmonic potential exists due to interactions with the confining walls [23,24], volume exclusion interac-

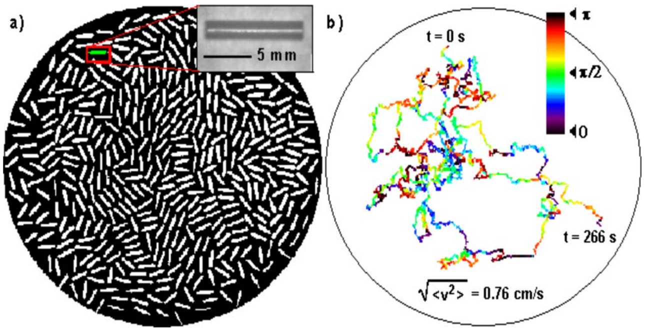

FIG. 1. (Color online) A monolayer of gas-fluidized bipolar rods. The diameter of the system is 17 cm. (a) A frame capture of the system from the video data after thresholding. The particles are plastic dowel pins—length of 0.95 cm, width of 0.24 cm, and mass of 0.055 g—occupying an area fraction of 42%. The call out shows an actual particle. (b) A time trace of one particle's motion (highlighted in the left image) in the presence of other particles. The color code corresponds to instantaneous orientation with respect to the horizontal axis of the image.

tions, and the turbulent, chaotic mixing of individual particle wakes overwhelms interactions with the boundaries and eliminates this external potential. Excluded volume interactions also serve to prevent unidirectional whirling of the particles.

In-plane motion of the rods is excited by a spatially and temporally uniform upflow of air at speed $U=370$ cm/s as measured by a hot-wire anemometer. The flow rate is uniform within ± 10 cm/s and on a time scale of 0.5 s. This is lower than the terminal free-fall speed for a horizontal rod so the rods do not levitate or fully lift off the plane. It is also low enough that the rods do not "chatter" [25]. Instead, one end of the rod lifts slightly off the plane and causes the rod to scoot preferentially in the direction of the tilt. In addition to scooting, the upflow of air also induces random short-time motion. Since the Reynolds number based on rod length and air speed is large, $\sim 10^3$, there is turbulence in the form of irregular wakes shed by the rods. The shedding frequency f_v is given by a universal value of the Strouhal number: $\mathrm{St}=f_v L/U=0.18$; a new wake is generated every time the air flows a distance of about $5L$ [26]. Therefore, the rods experience a corresponding random kicking force that fluctuates on a time scale $\tau_v=1/f_v\approx 0.018$ s [23].

The apparatus itself, fluidization method, and lighting setup are identical to those of Refs. [23,24]. The apparatus is a rectangular wind box, $1.5\times 1.5\times 4$ ft^3, positioned upright. A circular brass testing sieve with mesh size of 150 μm and diameter of 30.5 cm rests horizontally on top. To reduce alignment of the particles with the wall, we place the particles in a free-standing cylindrical insert, inner diameter of 17 cm and thickness of 0.32 cm, at the center of the larger bed. A blower attached to the wind box base provides vertical airflow perpendicular to the sieve. The upper and lower halves of the wind box are separated by a 1-inch-thick foam filter between two perforated metal sheets to eliminate large-scale structures in the airflow. Raw video data of the fluidized particles is captured for 10 min at 120 frames per second by a digital camera mounted above the apparatus. Postprocessing of the video data is accomplished using LABVIEW.

Figure 1(b) shows a sample time trace, $\{x(t),y(t),\theta(t)\}$, of a single particle. The color code denotes the instantaneous orientation of the particle with respect to the horizontal axis. The motion appears heterogeneous: we note several long stretches where the particle is preferentially moving parallel to its long axis. Apart from these, the wandering of the particle is like that of an isotropic particle undergoing a random walk. To obtain this time trace, we convert each frame of the raw data to binary as it is saved to video from buffer. Using LABVIEW's "IMAQ Particle Analysis" algorithm, we locate the centroid of each particle in the thresholded image, imposing an upper bound on the allowable area of a single particle, and determine the orientation of each particle with respect to a fixed horizontal axis. Any particles identified above the area bound consist of two or more particles that have collided. In order to distinguish the individual particles, a series of image processing steps known as erosions, similar to Ref. [25], is carried out. Figure 1(a) shows the result of the erosion process for one frame in which all particles have been separated.

Next, we link together particle positions and orientations from frame to frame by finding the minimum displacement between two center-of-mass positions in subsequent frames. To ensure correct matches, we constrain this with a maximum allowable displacement and rotation. The resulting time traces are then smoothed by a running average. We estimate error in the position and angle data as $\sigma_{\mathrm{rms}}/\sqrt{N}$, where σ_{rms} is the rms deviation of the raw data from the smoothed data and N is the number of frames in the smoothing window. This yields errors of 18 μm and 3.3 mrad in the position and angle data, respectively. Finally, to further minimize any wall effects, we include only those segments for which the particles are at least three particle diameters away from the wall.

III. SELF-PROPULSION

As noted in Sec. II, the sample time trace, Fig. 1(b), shows long stretches where particle orientation is aligned with the direction of motion, indicating scooting motion. To quantify this self-propelling behavior, we obtain the distributions of kinetic energies for motion parallel and perpendicular to the rod's long axis, and for the rod's orientation, shown in Fig. 2. We immediately see that equipartition of energy does not hold: at large energies, the distribution of parallel kinetic energies is much greater than the perpendicular distribution. The parallel component, with average value $\langle K_\parallel\rangle=1/2m\langle v_\parallel^2\rangle\sim 0.021$ ergs, is roughly twice as energetic as the perpendicular component, with $\langle K_\perp\rangle=1/2m\langle v_\perp^2\rangle\sim 0.012$ ergs. The rotational kinetic energy splits the difference between the two. Its average value is roughly the average of these two: $\langle K_\theta\rangle=1/2I\langle\omega^2\rangle\sim 0.016$ ergs, where we have used $I=(m/12)[3(d/2)^2+L^2]$. This shows that the gas-fluidized rods convert energy provided by the upflow of air into in-plane motion, preferentially parallel to the long axis. They do so at the expense of motion perpendicular to the rod's long axis. Such microscopic dynamical anisotropy—to which the emergence of collective macroscopic behavior has

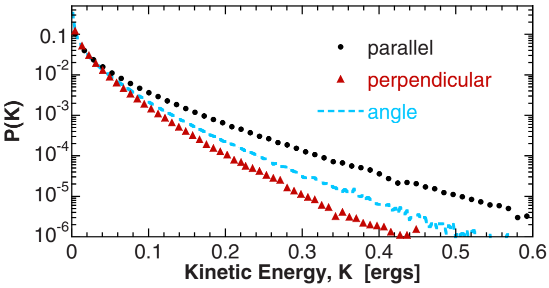

FIG. 2. (Color online) Distributions of kinetic energies, $K_{\parallel}$ and $K_{\perp}$, for motion parallel to and perpendicular to the particle's long axis and K_{θ}, the rotational kinetic energy. The average kinetic energy for each components is $\langle K_{\parallel}\rangle = 0.021$ ergs, $\langle K_{\perp}\rangle = 0.012$ ergs, and $\langle K_{\theta}\rangle = 0.016$ ergs. The kurtosis excess of the velocity distributions are 0.5 for parallel, 0.4 for perpendicular, and 0.6 for angle. A Gaussian distribution has a kurtosis excess of zero.

been attributed [15]—is a universal feature of theories and simulations of self-propelled particles, even when the anisotropy is not specified as a part of the model *a priori*. We can rightly consider our gas-fluidized rods in the context of self-propelled particles.

We also obtain the average self-propelling velocity, $v_{\parallel} \sim 0.87$ cm/s, from $\langle K_{\parallel}\rangle$. From this and the laboratory-frame diffusion coefficients D_x and D_{θ} to be discussed in Sec. V, we calculate $\alpha = v_{\parallel}^2/(D_x D_{\theta}) = 27$, a dimensionless parameter that determines the extent to which self-propulsion dominates over stochastic fluctuations [12]. For values $\alpha > 4$, self-propulsion dominates. Thus, we are clearly in a regime where self-propulsion effects will be readily observable. Furthermore, we can quantify the spatial and temporal extent of the "scooting" behavior by calculating an alignment order parameter $m(t) = \cos[\theta(t) - \phi(t)]$, the cosine of the angle between the particle's instantaneous orientation, $\theta(t)$, and the direction of its instantaneous velocity, $\phi(t)$. This quantity is one if a particle moves in the same direction that it is pointing and zero if it moves perpendicular to its orientation. Here, $\langle m\rangle = 0.46$ and $\sqrt{\langle m^2\rangle} = 0.75$. From the autocorrelation $\langle m(t) \cdot m(t+\tau)\rangle$, we extract a correlation time of 6.4 s. We quantify the spatial extent of the stretches from the value of the mean-square parallel displacement at the correlation time. This gives a displacement of 1.6 cm, roughly one-particle length per correlation time.

Self-propulsion is a strictly nonthermal phenomenon. The shape of the energy distributions in Fig. 2 further indicates the nonthermal character of our system. All of the distributions deviate sharply from an exponential at small energies. This sharp maximum has been observed for a single rod bouncing on a vibrated surface [27]. This is due to a strong correlation mentioned earlier between translation and rotation. Specifically, when the particle tilts out of plane and self-propels, its in-plane rotation is significantly reduced, and vice versa. The nonexponential form indicates that the velocity distributions are non-Gaussian. We confirm this by calculating a non-Gaussian parameter—the kurtosis excess, $\langle v^4\rangle/\langle v^2\rangle^2 - 3$, which equals zero for Gaussian distributions—of the velocity distributions. With kurtosis values of 0.6 for the angle, 0.5 for the parallel, and 0.4 for the perpendicular, none of the velocity distributions are Gaussian.

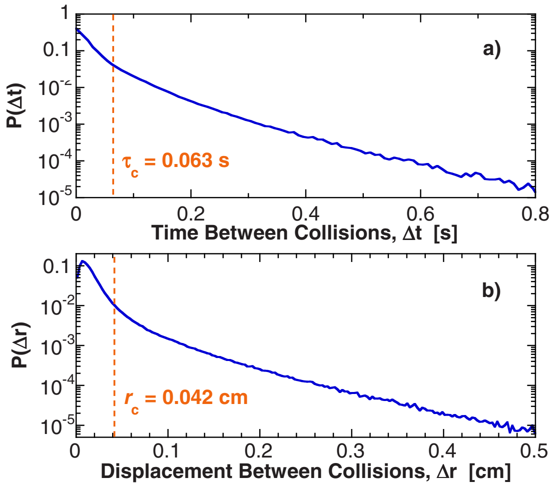

FIG. 3. (Color online) Probability distribution of (a) times between collisions and (b) displacements between collisions. The mean-free time, $\tau_c \sim 0.063$ s, and mean-free path, $r_c \sim 0.042$ cm, are labeled.

IV. COLLISIONS

The anisotropy of particle shape gives rise to self-propelled behavior and also alters the excluded volume interaction between particles. As a first step toward understanding these steric interactions, we compile binary collision statistics. We generate distributions of free times and free paths between collisions, shown in Fig. 3, using a graphical approach. We create a particle template that is the size of a grain had it not undergone any erosions or thresholding during data postprocessing. Then, we reconstruct each frame of the video by overlaying the template at the center of mass of each actual particle and rotating it by the particle's orientation. By detecting particle overlap, we determine whether a given particle has collided with any neighbors in a given frame. We then extract the time increment, Δt, and displacement, Δr, between collisions for a given particle, and compile them as probability distributions of free times, Fig. 3(a), and free paths, Fig. 3(b).

Although the tails of the distributions in Fig. 3 behave exponentially, there is substantial deviation at short times and paths. As such, we obtain well-defined mean values by taking the average of all the data rather than from an exponential fit. This yields a mean-free time between collisions, $\tau_c \sim 0.063$ s, and a mean-free path, $r_c \sim 0.042$ cm, marked as the dashed vertical lines in the figure. The ratio, $r_c/\tau_c = 0.67$ cm/s, is near the rms velocity, 0.76 cm/s. On subsequent dynamic plots, we mark the collision time with an orange dashed vertical line.

For thermal, isotropic systems, collisions are independent events; we expect exponential distributions for free paths and free times. The deviation of the distributions in Fig. 3 from exponential behavior at short times and paths further indicates nonthermal behavior. Distributions similar to ours were observed for spherical grains vibrated on an inclined plane [28]. There, the sharp maximum was attributed to inelastic clustering. Here, it may be attributable to local alignment—which may make a subsequent collision dependent on prior

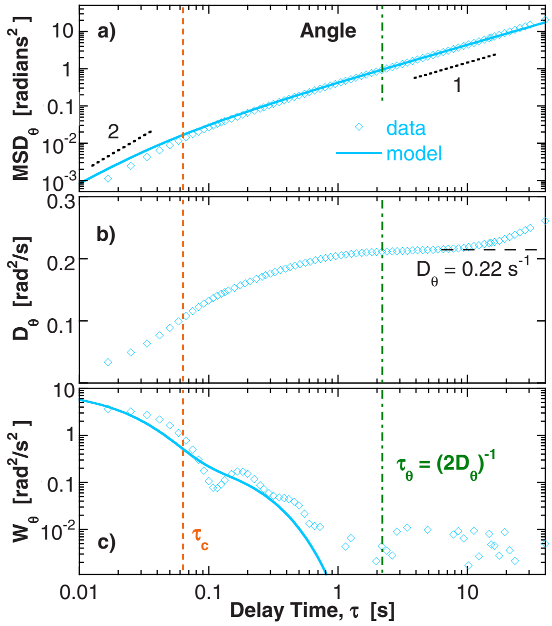

FIG. 4. (Color online) Dynamics of rod orientation: (a) mean-square angular displacement, (b) angular diffusion coefficient $D_\theta = \langle[\theta(t+\tau)-\theta(t)]^2\rangle/(2\tau)$, and (c) angular velocity autocorrelation function. The line with slope 1 in (a) corresponds to late-time diffusive motion; the line with slope 2 shows short-time ballistic motion. The horizontal line in (b) is the rotational diffusion coefficient, $D_\theta = 0.22\ \text{s}^{-1}$. The dashed vertical line (orange) marks the collision time, τ_c; the dash-dot line (green) marks the directional memory time, $\tau_\theta = (2D_\theta)^{-1}$. The solid curves are a Langevin model using a nonthermal noise source, given by Eqs. (7) and (8).

collisions—or to dynamical anisotropy. That is, a particle may be more likely to collide at short times as it propels through its environment.

V. LAB FRAME DYNAMICS

Despite being driven far from equilibrium, one or two gas-fluidized spheres act as Brownian particles in a harmonic trap [23]. However, in Sec. III, we showed that a rod moves more energetically parallel to its long axis and this thermal analogy subsequently fails. Here, we further ask how does self-propulsion alter the dynamics of a gas-fluidized rod? We begin by calculating single-particle dynamics in the laboratory frame where particle motion is characterized by both angular and translational displacements. The laboratory-frame axes, x and y, correspond to the horizontal and vertical axes of the raw images; angular orientation is measured counterclockwise with respect to $+x$. Recall from Sec. II that we only analyze data for which a particle is within three particle diameters from the wall, effectively breaking a single time trace into many shorter time traces. A typical particle moves across the system in less than a minute. Therefore, dynamical quantities, such as the mean square angular displacement, are truncated for delay times greater than 40 s.

Figure 4(a) shows the rotational mean-square displacement (MSD), $\langle[\theta(t+\tau)-\theta(t)]^2\rangle$, as a function of delay time τ. We observe ballistic behavior ($\propto\tau^2$) at the shortest time scales and a crossover to diffusive behavior ($\propto\tau$) at long times.

Rotational diffusion, characterized by the rotational diffusion coefficient $D_\theta(\tau) = \langle\Delta\theta^2(\tau)\rangle/(2\tau)$ shown in Fig. 4(b), sets a "directional memory" time scale $\tau_\theta = (2D_\theta)^{-1}$. At times greater than τ_θ, a particle will have forgotten its initial direction and all directions become equal. The long-time value of the angular diffusion coefficient, $D_\theta = 0.22\ \text{s}^{-1}$, is obtained from the plateau in Fig. 4(b), giving the value $\tau_\theta \sim 2.27$ s, shown as the vertical (green) dashed line in Fig. 4.

Chiral particles subject to external forces, such as those arising from the vibration of a substrate [29] or from air flowing past them as in the current experiment, spin in a preferred direction determined by the sign of their chirality. Small manufacturing defects impart chirality with a random sign and magnitude to some of the rods in this experiment. Some of the long-time rise in $D_\theta(\tau)$ is due to the spinning of some particles throughout the entire data set. If these particles are removed, an increase in slope is still detected, indicating heterogeneous dynamics for nonwhirling particles. Just as the time trace in Fig. 1(b) shows regions where particle scooting is intermittent with thermal-like wiggling, plots of $\theta(t)$ show regions of fluctuating motion intermittent with rapid rotation. We stress that, if we exclude whirlers, the long-time value of D_θ, and thus the time scale τ_θ, does not change significantly.

The angular velocity autocorrelation, $W_\theta(\tau) = \langle\omega(t+\tau)\cdot\omega(t)\rangle$, plotted in Fig. 4(c), shows a two-step decay, characterized by a large positive rebound near τ_c due to collisions, followed by small oscillations at longer times before noise dominates. The behavior of $W_\theta(\tau)$ at τ_c allows us to deduce the effect that collisions have on the particle. Typically, a collision results in a negative rebound: the particle recoils in a direction opposite to its incident direction. The large positive rebound in $W_\theta(\tau)$ suggests that the nature of our collisions is to realign the particle as to its initial direction.

We compute the translational dynamics in the laboratory frame, shown in Fig. 5. There is no discernible difference between data along x and y; only data along x is plotted. Figure 5(a) shows the laboratory-frame mean-square displacement, $\langle[x(t+\tau)-x(t)]^2\rangle$. The behavior is ballistic at short times and becomes diffusive at longer times. This is confirmed in Fig. 5(b): the laboratory-frame diffusion coefficient, $D_x(\tau) = \langle\Delta x^2(\tau)\rangle/(2\tau)$, approaches its long-time value, $D_x = 0.128$ cm/s, at about 10 s. The laboratory-frame velocity autocorrelation function, $W_x(\tau)$, shown in Fig. 5(c), has slower-than-exponential decay with a small wiggle at τ_c. Long-time statistics are poorer and the rebound at τ_θ may or may not be real.

Unexpectedly, equipartition of energy holds between the laboratory frame and the angle. From $W_x(0)$ and $W_\theta(0)$, we find that $(1/2)m\langle v_x^2\rangle \sim 0.017$ ergs, and $(1/2)I\langle\omega^2\rangle \sim 0.016$ ergs. That is, both the rotational and translational degrees of freedom in the laboratory frame have the same kinetic energy. Remarkably, despite the self-propelled nature of the particles, if one averages over all possible orientations, the resulting bulk behavior appears thermal. This is consistent with the results in Fig. 2; the distribution of kinetic

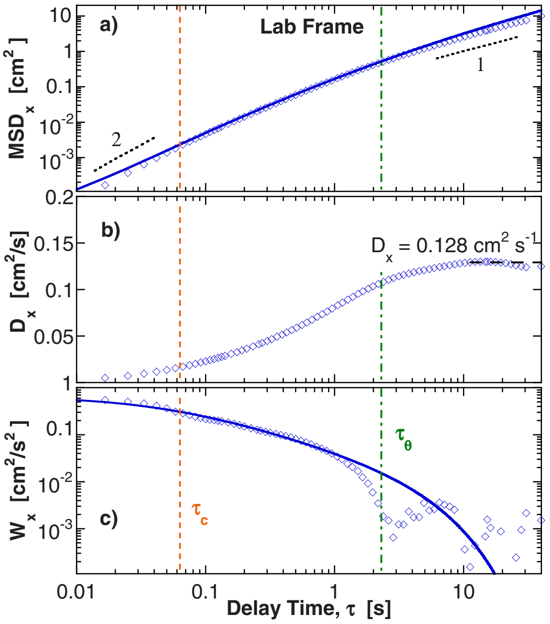

FIG. 5. (Color online) Dynamics of rod position in the laboratory frame: (a) mean-square displacement, (b) diffusion coefficient $D_x = \langle [x(t+\tau) - x(t)]^2 \rangle / (2\tau)$, and (c) velocity autocorrelation function. The horizontal line in (b) shows the long-time value of the diffusion coefficient, $D_x = 0.128$ cm s^{-1}. The dashed vertical line (orange) marks the collision time, τ_c; the dash-dot line (green) marks the directional memory time, $\tau_\theta = (2D_\theta)^{-1}$. The solid curves are a Langevin model using a nonthermal noise source, given by the first term in Eq. (13).

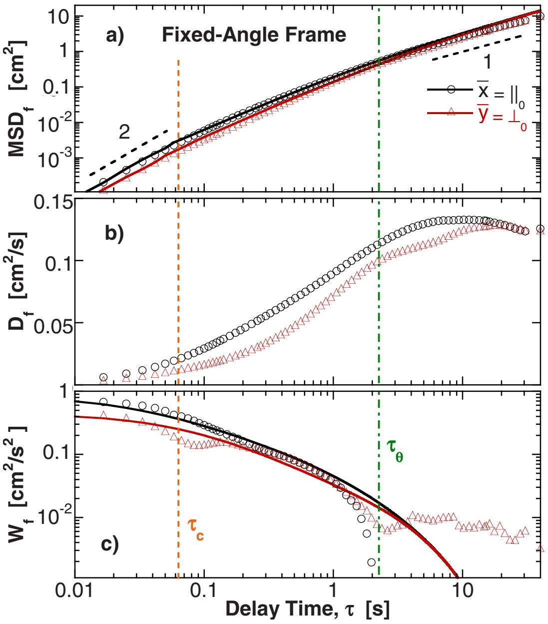

FIG. 6. (Color online) Dynamics of rod position in the fixed-angle laboratory frame: (a) mean-square displacement, (b) diffusion coefficient, and (c) velocity autocorrelation function. At $t=0$, $\bar{x}$ is aligned parallel to the particle's long axis. The dashed vertical line (orange) marks the collision time, τ_c; the dash-dot line (green) marks the directional memory time, $\tau_\theta = (2D_\theta)^{-1}$. The solid curves are a Langevin model using nonthermal noise sources, given by Eq. (13).

energies in the laboratory frame is nearly identical to that of the angle, and the average of the parallel and perpendicular distributions.

VI. COUPLING ROTATION AND TRANSLATION

In this section, we ask how do rotation and translation couple for a self-propelling particle? To explicitly visualize rotational-translational coupling, we calculate the dynamics in a "fixed-angle" laboratory frame with axes $\bar{x}$ and $\bar{y}$. We construct this frame by rotating the coordinates of an entire time trace by the initial particle orientation so that $\bar{x}$ and $\bar{y}$ are, respectively, parallel and perpendicular to the initial direction of the long axis of the particle. The axes then remain fixed in time. This is equivalent to setting the initial orientation of all particles to $\theta_0 = 0$.

For comparison purposes, it is instructive to review how rotation and translation couple for a Brownian particle [20–22]. If a particle is not allowed to rotate, translational motion is characterized by anisotropic diffusion—with two diffusion coefficients, $D_\parallel$ and $D_\perp$—for displacements parallel and perpendicular to the particle's long axis. The two components, it should be noted, become diffusive on the same time scale. If the particle is allowed to rotate, this anisotropic diffusion regime will cross over to isotropic diffusion characterized by a single diffusion coefficient, $D_x = (1/2)(D_\parallel + D_\perp)$. The crossover time scale is the same directional memory time scale discussed earlier in Sec. V, $\tau_\theta = (2D_\theta)^{-1}$. Thus, at times longer than τ_θ, the fixed-angle laboratory-frame axes will become random, and the dynamics along $\bar{x}$ and $\bar{y}$ will become equivalent to the conventional laboratory frame, x and y.

The fixed-angle laboratory-frame mean-square displacements $\langle \Delta \bar{x}^2(\tau) \rangle$ and $\langle \Delta \bar{y}^2(\tau) \rangle$, Fig. 6(a), are both ballistic at short times. This short-time behavior confirms the discussion in Sec. III that equipartition of energy does not hold, with $\langle \Delta \bar{x}^2(\tau) \rangle$ twice as large as $\langle \Delta \bar{y}^2(\tau) \rangle$. After τ_θ, the fixed-angle MSDs become diffusive and eventually converge, showing that the coordinate axes are randomized and the particle has forgotten its initial direction. This indicates coupling between rotation and translation in our system. However, examining Fig. 6(b), we do not observe a fully developed anisotropic diffusion regime. Instead, following the initial anisotropic ballistic regime, $\bar{D}_x$ indicates diffusion at approximately 6 s but $\bar{D}_y$ does not become diffusive until about 20 s. Isotropic diffusion occurs near 20 s, when the two diffusion coefficients converge.

We see that coupling for self-propelled particles is different than Brownian in two significant ways. First, the intermediate-time dynamics show that the two components become diffusive on different time scales. Recalling the ballistic-to-diffusive time scale for the conventional orientation-averaged laboratory frame, $\bar{x}$ becomes diffusive sooner and $\bar{y}$ later. This is most likely because the parallel component is more energetic than the perpendicular component; thus, it takes longer for the $\bar{y}$ component to "catch up" and become equal to $\bar{x}$. Second, isotropic diffusion occurs at

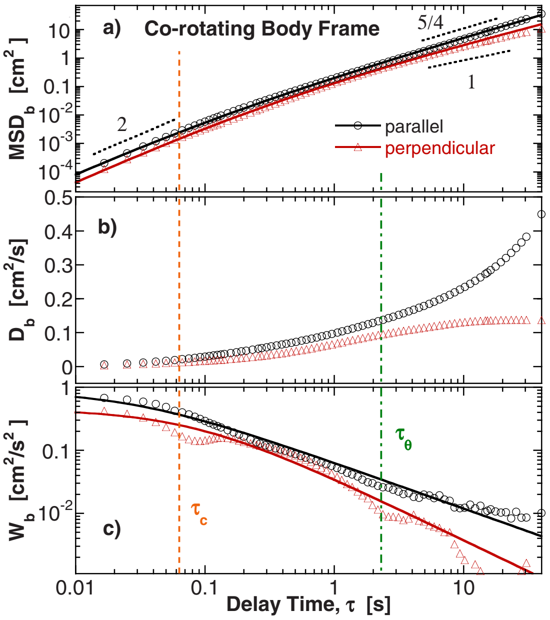

FIG. 7. (Color online) Dynamics of rod position in the body frame: (a) mean-square displacement MSD$_b$, (b) diffusion coefficient, and (c) velocity autocorrelation function. The corotating body-frame axes are always either parallel or perpendicular to the particle's long axis. The line with slope 5/4 in (a) corresponds to superdiffusive motion. The dashed vertical line (orange) marks the collision time, τ_c; the dash-dot line (green) marks the directional memory time, $\tau_\theta=(2D_\theta)^{-1}$. The solid curves are a Langevin model using a nonthermal noise source, given by Eqs. (10) and (11).

a time scale an order-of-magnitude larger than τ_θ. Thus, we think of self-propulsion as a "memory enhancement" effect. Isotropic diffusion occurs much later because self-propulsion, in effect, allows the particle to remember its initial direction for a longer time.

VII. BODY FRAME DYNAMICS

While the fixed-angle laboratory frame is useful for illustrating the effects of self-propulsion at short and intermediate times, it is useful to consider yet another reference frame to capture the effects at longer times. The body frame is a set of axes, $\tilde{x}$ and $\tilde{y}$, which are reoriented at each time step to coincide with the long and short dimensions of each rod, respectively. The individual displacements are then summed up successively to form a set of time traces, $\{\tilde{x}(t),\tilde{y}(t)\}$. Here, $\theta(t)=0$ at all times and there is no coupling in this frame.

At short times, the body-frame mean-square displacements in Fig. 7(a) are identical to the fixed-angle laboratory-frame-square displacements of Fig. 6(a). At long times, $\langle\Delta\tilde{y}_\perp^2(\tau)\rangle$ crosses over to diffusive behavior whereas $\langle\Delta\tilde{x}_\parallel^2(\tau)\rangle$ becomes superdiffusive ($\propto\tau^{5/4}$). Self-propulsion gives rise to enhanced diffusion for translations along the particle's long axis. As seen in Fig. 7(b), the perpendicular diffusion coefficient, $D_\perp$, has reached its long-time value while $D_\parallel$ continues to increase.

The body-frame velocity autocorrelation functions, $W_\parallel(\tau)$ and $W_\perp(\tau)$, shown in Fig. 7(c), reveal the long memory of the particle motion. The perpendicular component has a slow decay that exhibits the same rebounding features at τ_c and τ_θ as seen in $W_\theta(\tau)$ and $W_x(\tau)$. The parallel component shows a smooth slower algebraic decay for the entire run indicating remarkably long-lived velocity correlations. This is consistent with the long unbroken stretches of scooting motion seen in the time-trace image, Fig. 1(b).

VIII. MODEL

Collections of self-propelled particles are typically modeled in one of two ways: establishing a minimal set of rules [1,2] or writing hydrodynamic equations, including all terms consistent with relevant symmetries [3–5]. Self-propulsion is usually included as a phenomenological parameter. In keeping with such minimal models, we describe our system with a Langevin formalism constructed along the lines of that for an anisotropic Brownian particle. We make a single modification: rather than write a self-propelling force, we implicitly include self-propulsion with nonthermal noise terms. We begin by constructing Langevin equations for the three independent degrees of freedom—the angle and the two body-frame components.

The effective harmonic potential of the bed has been eliminated and there are no externally imposed forces or torques. The remaining forces—arising from interparticle collisions, interactions with the substrate, and hydrodynamic interactions with wakes—can be considered as noise. Thus, our Langevin equations simply relate time derivatives of angle and displacement to random-noise torques and forces. The equation for the orientation of the rod, $\theta(t)$, is

$$\frac{d\theta}{dt}\equiv\omega(t)=\zeta_\theta(t), \tag{1}$$

where $\zeta_\theta(t)$ is Gaussian angular noise with zero average and variance

$$\langle\zeta_\theta(t)\zeta_\theta(t')\rangle=\langle\omega(t)\omega(t')\rangle\equiv W_\theta(\tau). \tag{2}$$

From Eq. (1), $W_\theta(\tau)$ is the velocity autocorrelation function of Fig. 4(c).

The equations for displacement can be expressed in the laboratory frame $\mathbf{x}_{\text{lab}}(t)=\{x(t),y(t)\}$ or in the body frame, $\tilde{x}(t)=\{\tilde{x}(t),\tilde{x}(t)\}$. In the body frame, $\tilde{x}(t)$ and $\tilde{y}(t)$ decouple:

$$\frac{d\tilde{x}}{dt}\equiv\tilde{v}_x(t)=\zeta_\parallel(t), \tag{3}$$

$$\frac{d\tilde{y}}{dt}\equiv\tilde{v}_y(t)=\zeta_\perp(t), \tag{4}$$

where $\zeta_\parallel(t)$ and $\zeta_\perp(t)$ are Gaussian random noises with zero mean and variance

$$\langle\zeta_\parallel(t)\zeta_\parallel(t')\rangle=\langle v_\parallel(t)v_\parallel(t')\rangle\equiv W_\parallel(\tau), \tag{5}$$

$$\langle\zeta_\perp(t)\zeta_\perp(t')\rangle=\langle v_\perp(t)v_\perp(t')\rangle\equiv W_\perp(\tau). \tag{6}$$

The noises $W_\perp(\tau)$ and $W_\parallel(\tau)$ are the body-frame velocity autocorrelation functions of Fig. 7(c).

The Langevin equations derived above apply to both equilibrium and nonequilibrium systems. In equilibrium systems, the noise fluctuations of Eqs. (2), (5), and (6) are determined by the fluctuation-dissipation theorem. They adopt white-noise forms when rotational and translational friction coefficients do not exhibit memory effects. Nonequilibrium systems are not restricted by the fluctuation-dissipation theorem. Here, we use the experimental forms of the angular and translational velocity autocorrelation functions to set $W_\theta(\tau)$, $W_\perp(\tau)$, and $W_\parallel(\tau)$. Since these quantities contain all the information about self-propulsion, we are able to implicitly include self-propulsion in our model via nonthermal noise. We will then be able to test whether modeling self-propulsion as nonthermal noise is sufficient in lieu of specifying an actual force acting along the long axis of the particle.

The form of the angular noise $\zeta_\theta(t)$ can be determined from the two-step decay of $W_\theta(\tau)$, Fig. 4(c). This suggests that the simplest functional form is the sum of two exponentials:

$$W_\theta(\tau) = D_\theta\left(\frac{a}{\tau_1}e^{-|\tau|/\tau_1} + \frac{1-a}{\tau_2}e^{-|\tau|/\tau_2}\right), \tag{7}$$

where a is a real number between zero and one. The fit to Eq. (7), shown as the solid curve in Fig. 4(c), was made by constraining D_θ to equal its long-time value, $0.22\ \mathrm{s}^{-1}$, rather than using it as a fitting parameter. Although unable to capture the sharp rebound caused by collisions, Eq. (7) provides a good fit to $W_\theta(\tau)$. We stress that this form is not a prediction of our model but rather the simplest functional form that describes the data well. We extract two correlation times: $\tau_1 = 0.018 \pm 0.005$ s and $\tau_2 = 0.11 \pm 0.01$ s. The smaller correlation time is identical to the vortex shedding time scale τ_ν calculated in Sec. II. The value of τ_2 is roughly the collision time.

We also calculate the analytical form of the mean-square angular displacement:

$$\langle(\Delta\theta)^2\rangle = 2D_\theta[aS(t-t',\tau_1) + (1-a)S(t-t',\tau_2)], \tag{8}$$

where we define

$$S(t,\tau) = |t| - \tau(1 - e^{-|t|/\tau}). \tag{9}$$

Using the fit values from Eq. (7), we plot Eq. (8) as the solid curve in Fig. 4(a). As a consequence of constraining the value of D_θ when fitting to Eq. (7), the result overestimates the value of the MSD at short times.

The form of the body-frame noise, $\zeta_\parallel(t)$ and $\zeta_\perp(t)$, is obtained from $W_\parallel(\tau)$ and $W_\perp(\tau)$, Fig. 7(c), respectively. The slow decay suggests a power-law form:

$$W_i(\tau) = \frac{A_i}{(1+b_i\tau)^{\alpha_i}}. \tag{10}$$

The solid curves in Fig. 7(c) are fits to Eq. (10), yielding exponents of $\alpha_\perp = 0.99 \pm 0.04$ and $\alpha_\parallel = 0.73 \pm 0.02$. These terms implicitly include the two nonthermal effects of self-propulsion. First, the magnitudes, A_i, contain information about the energy gap between the two components. Second, the power-law exponents incorporate the extended memory effect of self-propulsion. We note that a power-law decay, $\tau^{-d/2}$, is expected for particles suspended in a fluid due to diffusive transport of momentum through the surrounding fluid [30]. Although this is not the case for our study, we highlight it as a potential analogy: particles in a viscous medium and self-propelling particles both exhibit velocity autocorrelations with extended memory effects. This form is also able to capture the superdiffusive behavior of $\langle\Delta\tilde{x}_\parallel^2(\tau)\rangle$. We obtain the following expression for the body-frame mean-square displacements:

$$\langle(\Delta\tilde{x}_i)^2\rangle = \frac{2A_i}{(1-\alpha_i)(2-\alpha_i)b_i^2}[(a_i + b_i\tau)^{2-\alpha_i} - a_i^{2-\alpha_i}] - \frac{2A_i}{(1-\alpha_i)b_i}a_i^{1-\alpha_i}\tau. \tag{11}$$

This form shows a crossover from τ^2 at short times to $\tau^{2-\alpha_i}$ at long times. Using the parameters obtained from the fit to Eq. (10), we plot the functional forms given by Eq. (11) as the solid lines in Fig. 7(a).

We now have enough information to construct the coupled fixed-angle laboratory-frame dynamics. Writing the velocity in the fixed-angle laboratory frame in terms of the body-frame velocity,

$$\bar{v}_k(t) = R_{kl}^{-1}[\theta(t)]\tilde{v}_l(t), \tag{12}$$

we obtain for the fixed-angle laboratory-frame velocity autocorrelation function:

$$W_f(t,t') = \frac{1}{2}[W_\parallel(\tau) + W_\perp(\tau)]e^{-\langle(\Delta\theta)^2\rangle/2}\delta_{ij} + \frac{1}{2}[W_\parallel(\tau) - W_\perp(\tau)]M_{ij}[\theta(0)]e^{-\langle[\theta(t')+\theta(t)]^2\rangle/2}, \tag{13}$$

where $\theta(0)=0$ and

$$M_{ij} = \begin{pmatrix} \cos 2\theta(t) & \sin 2\theta(t) \\ \sin 2\theta(t) & -\cos 2\theta(t) \end{pmatrix}. \tag{14}$$

We use the fitting parameters obtained from our fits to Eqs. (7) and (10) to generate Eq. (13), plotted as the solid curves in Fig. 6(c). The model shows that $W_{\tilde{x}}(\tau)$ and $W_{\tilde{y}}(\tau)$ converge at τ_θ, consistent with a crossover in the data. The discrepancy between the model prediction and the data at long times may indicate that memory effects persist even longer than expected.

We then numerically integrate $W_f(t,t')$ according to

$$\langle[\Delta\bar{x}(t)]^2\rangle = \int_0^t dt_1 \int_0^t dt_2 W_f(t_1,t_2) \tag{15}$$

to obtain the solid curves in Fig. 6(a). The components of the model converge on the same time scale as the data. We see that modeling self-propulsion as an external noise source with long-lived correlations is sufficient to reproduce rotational-translational coupling. Our model suggests that a phenomenological way to think about collections of self-propelling particles is in terms of enhanced memory effects rather than explicitly detailing novel forces and torques in microscopic equations.

The model also reproduces the angle-averaged laboratory-frame dynamics well (Fig. 5). Averaging our expressions over all initial angles eliminates the second term in Eq. (13); the result is plotted in Fig. 5(c) as the solid curve. We integrate according to Eq. (15) to obtain the solid curve in Fig. 5(a). The model describes the angle-averaged velocity correlations very well up to 1 s, after which the data falls off more rapidly. The good agreement with the fit here confirms the bulk thermal behavior of the collection of self-propelling rods.

IX. CONCLUSION

We have investigated the dynamics of gas-fluidized rods. Particle shape anisotropy leads to dynamical anisotropy, characterized by preferential motion parallel to the particle's long axis. Ours is a model system—with the advantage of a temporally and spatially homogeneous driving method—to further investigate universal phenomena predicted for collections of self-propelled particles.

In this report, we compared the coupling of rotation and translation couples for a self-propelled particle to that of an anisotropic Brownian particle. A modified Langevin formalism implicitly specifying self-propulsion via nonthermal noise describes the dynamics data well, capturing rotational-translational coupling at the correct time scale. Despite the energy gap between the parallel and perpendicular components, the model was able to reproduce the loss of directional memory at long times. Furthermore, despite the nonthermal behavior of individual particles, the bulk angle-averaged behavior is nearly thermal.

Future work will continue to explore phase space in the interest of observing collective behavior and spontaneous symmetry breaking for denser collections of both bipolar and polar self-propelled particles. We are interested in whether we can induce collective macroscopic behavior by manipulating the boundaries of the system as well. We are currently working on characterizing compression waves that propagate through denser collections of gas-fluidized rods. We hope that, through comparison with theoretical models [1–7,10–12] and recent vibrated-bed experiments [9,13–17], our system will further shed light on universal behavior of collections of self-propelled particles.

ACKNOWLEDGMENTS

We thank Adam Abate for helpful discussion and for programming assistance. This work was supported by the NSF through Grants No. DMR-0704147 and No. DMR-0804900.

[1] T. Vicsek, A. Czirok, E. Ben-Jacob, I. Cohen, and O. Shochet, Phys. Rev. Lett. **75**, 1226 (1995).

[2] G. Gregoire and H. Chate, Phys. Rev. Lett. **92**, 025702 (2004).

[3] J. Toner and Y. Tu, Phys. Rev. Lett. **75**, 4326 (1995).

[4] J. Toner and Y. Tu, Phys. Rev. E **58**, 4828 (1998).

[5] J. Toner, Y. Tu, and S. Ramaswamy, Ann. Phys. **318**, 170 (2005).

[6] S. Ramaswamy, R. A. Simha, and J. Toner, Europhys. Lett. **62**, 196 (2003).

[7] H. Chate, F. Ginelli, and R. Montagne, Phys. Rev. Lett. **96**, 180602 (2006).

[8] I. S. Aranson and L. S. Tsimring, Phys. Rev. E **67**, 021305 (2003).

[9] I. S. Aranson, D. Volfson, and L. S. Tsimring, Phys. Rev. E **75**, 051301 (2007).

[10] Y. Tu, J. Toner, and M. Ulm, Phys. Rev. Lett. **80**, 4819 (1998).

[11] R. Aditi Simha and S. Ramaswamy, Phys. Rev. Lett. **89**, 058101 (2002).

[12] A. Baskaran and M. C. Marchetti, Phys. Rev. E **77**, 011920 (2008).

[13] D. L. Blair, T. Neicu, and A. Kudrolli, Phys. Rev. E **67**, 031303 (2003).

[14] J. Galanis, D. Harries, D. L. Sackett, W. Losert, and R. Nossal, Phys. Rev. Lett. **96**, 028002 (2006).

[15] V. Narayan, N. Menon, and S. Ramaswamy, J. Stat. Mech.: Theory Exp. (2006) P01005.

[16] V. Narayan, S. Ramaswamy, and N. Menon, Science **317**, 105 (2007).

[17] A. Kudrolli, G. Lumay, D. Volfson, and L. S. Tsimring, Phys. Rev. Lett. **100**, 058001 (2008).

[18] I. S. Aranson, A. Snezhko, J. S. Olafsen, and J. S. Urbach, Science **320**, 612 (2008).

[19] V. Narayan, S. Ramaswamy, and N. Menon, Science **320**, 612 (2008).

[20] F. Perrin, J. Phys. Radium **5**, 497 (1934).

[21] F. Perrin, J. Phys. Radium **7**, 1 (1936).

[22] Y. Han, A. M. Alsayed, M. Nobili, J. Zhang, T. C. Lubensky, and A. G. Yodh, Science **314**, 626 (2006).

[23] R. P. Ojha, P. A. Lemieux, P. K. Dixon, A. J. Liu, and D. J. Durian, Nature (London) **427**, 521 (2004).

[24] R. P. Ojha, A. R. Abate, and D. J. Durian, Phys. Rev. E **71**, 016313 (2005).

[25] A. R. Abate and D. J. Durian, Phys. Rev. E **72**, 031305 (2005).

[26] S. Rajagopalan and R. A. Antonia, Exp. Fluids **38**, 393 (2005).

[27] H. S. Wright, M. R. Swift, and P. J. King, Phys. Rev. E **74**, 061309 (2006).

[28] D. L. Blair and A. Kudrolli, Phys. Rev. E **67**, 041301 (2003).

[29] J. C. Tsai, F. Ye, J. Rodriguez, J. P. Gollub, and T. C. Lubensky, Phys. Rev. Lett. **94**, 214301 (2005).

[30] B. F. Alder and T. E. Wainwright, Phys. Rev. Lett. **18**, 988 (1967).